Nanoscale

Accepted Manuscript

This article can be cited before page numbers have been issued, to do this please use: F. Tang, Z.C. Su, H. Ye, Y. Zhu, J. Dai and S. J. Xu, *Nanoscale*, 2019, DOI: 10.1039/C9NR07081H.

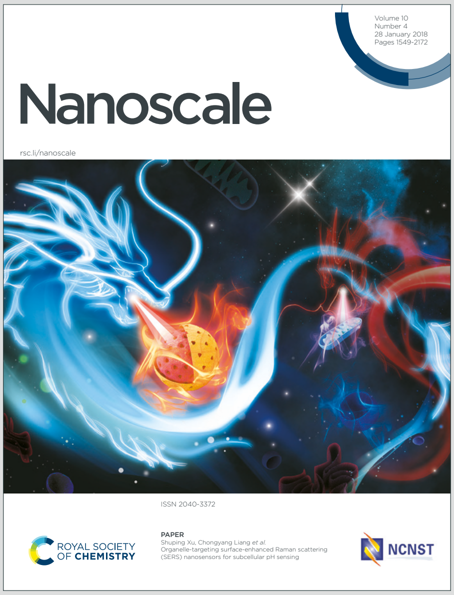

ROYAL SOCIETY OF CHEMISTRY

rsc.li/nanoscale

View Article Online
DOI: 10.1039/C9NR07081H

Anomalous variable-temperature photoluminescence of $CsPbBr_3$ perovskite quantum dots embedded into an organic solid

Fei Tang,[†, ‡] Zhicheng Su,[†] Honggang Ye,[†, §] Ye Zhu,[] Jiyan Dai,[] and Shijie Xu[*†]

[†]Department of Physics, and Shenzhen Institute of Research and Innovation (HKU-SIRI), The University of Hong Kong, Pokfulam Road, Hong Kong, China

[‡]Jiangsu Key Laboratory of Advanced Laser Materials and Devices, School of Physics and Electronic Engineering, Jiangsu Normal University, Xuzhou 221116, China

[§]Department of Applied Physics, Xi'an Jiaotong University, Xi'an 710049, China

[]Department of Applied Physics, The Hong Kong Polytechnic University, Hung Hom, Kowloon, Hong Kong, China

[*]E-mail: sjxu@hku.hk

Keywords: Perovskites, metal lead halide, quantum dots, photoluminescence

Abstract: All-inorganic lead halide perovskite quantum dots (PQDs) of $CsPbBr_3$ were synthesized at room temperature via a facile solution-based procedure. Cubic phase structure of the synthesized PQDs was judiciously identified through examining high-resolution transmission electron microscope (TEM) images, selected area electronic diffraction (SAED) patterns and scanning TEM images of the PQDs. Variable-temperature photoluminescence (PL) spectra of the $CsPbBr_3$ PQDs randomly embedded into a frozen solid of methylbenzene were measured in a temperature range of 5-180 K. It is found that both linewidth and peak position of the measured PL spectra are abnormally almost temperature independent in the interested temperature range. Some competing mechanisms, such as a competition between bandgap blue shift induced by thermal lattice expansion and red shift by thermal escaping of localized excitons, and a competition between lineshape broadening by phonon scattering and narrowing by thermal escaping of localized excitons, are proposed to interpret the phenomena. Good agreement between the theoretical fitting and the experimental data leads to a state-of-the-art understanding of the temperature-dependent luminescence of the $CsPbBr_3$ PQDs in solid matrix.

1. INTRODUCTION

In recent years, perovskite quantum dots (PQDs) have emerged as promising candidates for light harvesting and emitting materials mainly because of their extraordinary optical properties.[1–5] Among various PQDs, inorganic halide PQDs of $CsPbX_3$ are of particular interest due to their high luminescence quantum yield (QY) and large emission color tunability via controlling its composition and feature size.[6–10] Moreover, such all inorganic PQDs show much better chemical stability in comparison with their organic-inorganic hybrid counterparts. Currently, $CsPbBr_3$ PQDs are being extensively investigated as an outstanding example of all inorganic PQDs.[10–14] More interestingly, a recent theoretical study by Kang and Wang[15] reveals that pure inorganic $CsPbBr_3$ is highly defect tolerant because that most of the intrinsic defects induce shallow transition levels. Therefore, $CsPbBr_3$ perovskite can maintain its good electronic quality despite the presence of defects.[15] In fact, more-than-expected rich physics and chemistry as well as application potential have been recently discussed by Huang *et al*. for $CsPbBr_3$ perovskite, especially for nanostructures of $CsPbBr_3$ perovskite.[16] Among them are the crystalline structures and luminescence properties. Cottingham and Brutchey utilized X-ray diffraction and pair distribution function (PDF) analysis of X-ray total scattering data to indicate that the crystal structure of $CsPbBr_3$ PQDs is unequivocally orthorhombic (*Pnma*).[17] However, a more recent study by Brennan, Kuno, and Rouvimov on the atomic structure of $CsPbBr_3$ nanocubes shows some evidence for a size dependency to the crystal symmetry of $CsPbBr_3$ nanostructures.[18] For example, they found that the coexistence of both cubic ($Pm\bar{3}m$) and orthorhombic lattices may exist in $CsPbBr_3$ nanocubes with average edge length of ∼10 nm, whereas solely cubic character is observed in $CsPbBr_3$ nanocubes with ∼5 nm edge length. In fact, Yu and his co-workers obtained an earlier observation of the co-existence of cubic and orthorhombic phases in ultrathin two-dimensional $CsPbBr_3$ halide perovskites by combining aberration-corrected high-resolution transmission

View Article Online
DOI: 10.1039/C9NR07081H

electron microscopy (HRTEM) with exit-wave reconstruction simulation.[19] Such atomic resolution imaging measurements not only offer unprecedented opportunities to better understand halide perovskites at the atomic level, but also may gain critical insight into the structure-property relationship of $CsPbBr_3$ and other materials nanostructures.

On the other hand, surrounding environments may have significant impact on microstructure and properties of $CsPbBr_3$ nanostructures. For instance, He *et al*. recently demonstrated that inorganic $CsPbBr_3$ perovskite nanorods in a polymer matrix can have good dimensional control, outstanding optical properties and ultrahigh environmental stability.[20] Zhang *et al*. showed that silica coating can enhance stability and even luminescence quantum efficiency of $CsPbBr_3$ PQDs.[21] Obviously, an in-depth investigation of crystalline structure and variable-temperature photoluminescence (PL) of $CsPbBr_3$ PQDs is of scientific interest. In particular, a variable-temperature PL study on $CsPbBr_3$ PQDs embedded into an organic solid has not yet been reported and thus highly desirable for enhancing the existing understanding of luminescence mechanism of composite PQDs + surrounding solid. By using combined techniques of HRTEM + selected area electronic diffraction (SAED) + high angle annular dark-field scanning TEM (STEM), we obtain strong evidence for the cubic ($Pm\bar{3}m$) lattice phase in the synthesized $CsPbBr_3$ PQDs. More interestingly, it is found that both PL peak position and full-width at half maximum (FWHM) exhibit unusual behaviors, i.e., nearly independent on temperature in the interested temperature range when the PQDs are randomly embedded into a frozen methylbenzene solid. A compensating mechanism is proposed to quantitatively interpret the anomalies of two major spectral parameters in their temperature dependence for the $CsPbBr_3$ PQDs. Such a study thus may gain a deeper insight into the challenging thermal behaviors of luminescence of the PQDs embedded into a solid matrix.

2. RESULTS AND DISCUSSION

Figure 1(a) illustrates a schematic diagram of cubic crystalline structure of perovskite ABC_3 unit cell, where Cs^+ ions occupy the corner A-site and Pb^{2+} ions located at the body-center B-site. Br^- ions located at the face center C-sites serve as ligands surrounding the Pb^{2+} center ions. Figure 1(b) presents a low-resolution TEM image of the synthesized PQDs. In this low-magnification image, the PQDs assemble together and look like a polycrystalline collective body with irregular shapes and feature size of sub-micro meters. This phenomenon could be interpreted in terms of serious aggregation effect in the $CsPbBr_3$ PQDs under the conditions of high density. But, HRTEM image of individual PQDs shows a nearly perfect crystalline lattice structure, as seen in Figure 1(c). Regular crystalline planes are so clearly resolved that some interplanar spacings can be directly read out, i.e., 5.62 and 3.98 Å as marked in the HRTEM image. Two selected mutual rectangular regions denoted as I and II, respectively, shall correspond to the two different families of crystallographic planes. By measuring their interplanar spacings as shown in Figure 1(d), we may ascribe them to the (011) and (100) crystallographic planes in a cubic structure with space group of $Pm\bar{3}m$. To further support such assignment, we measured SAED patterns and high angle annular dark-field STEM image along the <011> zone-axis, as shown in Figure 2(a) and (c), respectively. By simulating the SAED patterns and examining the STEM image with atomic resolution, we may determine local atomic arrangement of a sample.[22,23]

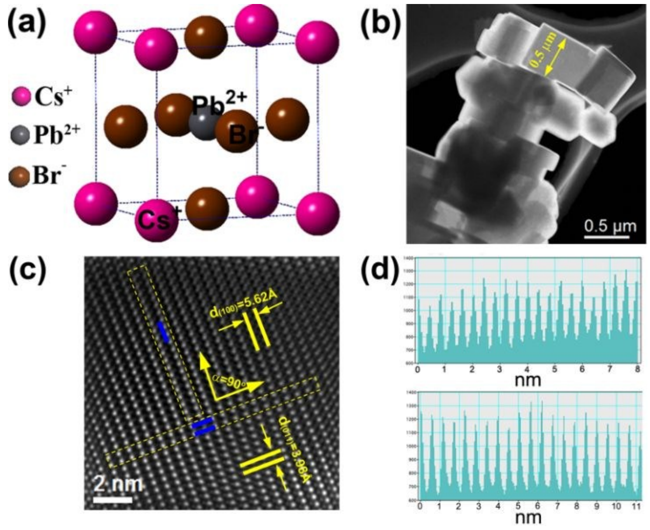

Figure 1. (a) Atomic structure model of the cubic $CsPbBr_3$ perovskite unit cell. (b) Low-resolution TEM image of the synthesized $CsPbBr_3$ PQDs. (c) HRTEM image of the synthesized $CsPbBr_3$ PQDs. (d) Contour profiles of region I (upper) and II (bottom) in (c). Interplanar spacings can be directly determined.

Figure 2(b) and (d) show the measured SAED patterns and STEM image along the zone-axis of <111>, respectively. Regularly distributed diffraction spots can be clearly observed in the SAED images (e.g. reciprocal space), indicating at least the local excellent lattice array in real space. In Figure 2(a), the entire diffraction patterns may be reconstructed with a unit structure of rectangle plane (yellow dashed), while the SAED patterns in Figure 2(b) can be rebuilt with a unit

View Article Online
DOI: 10.1039/C9NR07081H

structure of standard hexagon shape outlined by yellow dashed line. With a model of cubic atomic structure and single crystal simulation software,[24] the Miller index of each plane (e.g. each spot in the SAED image) can be determined, as marked in Figure 2(a) and (b). For the STEM images, we adopted the CrystalMaker Software[25] to simulate them. Figure 3(a) and (b) show the atomic structures (color balls) derived from the simulations to the SAED and STEM images overlaid on the amplified local HRTEM and STEM images, respectively. It is clearly seen that the derived atomic structures with a cubic phase match well with the experimental results. The excellent agreement between simulation and experiment provides strong evidence for the crystal structure identification that the synthesized PQDs possess a cubic structure rather than an orthorhombic phase. Compared to the latter, cubic phase may enable PQDs more stable and more efficient in luminescence due to high symmetric crystalline structure.

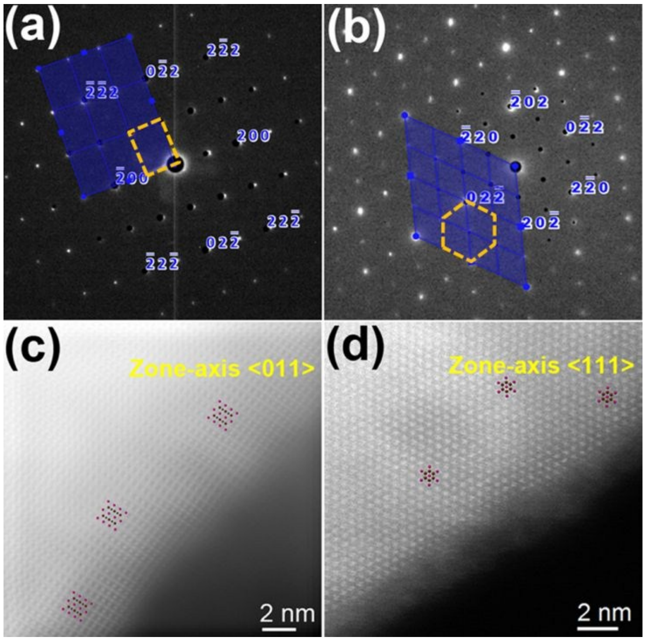

Figure 2. Experimental and simulated SAED patterns along the zone-axis of (a) <011> and (b) <111>. (c), (d) Measured STEM images along these two zone-axis directions. Derived two atomic structures (color balls) were overlaid on the STEM images, respectively.

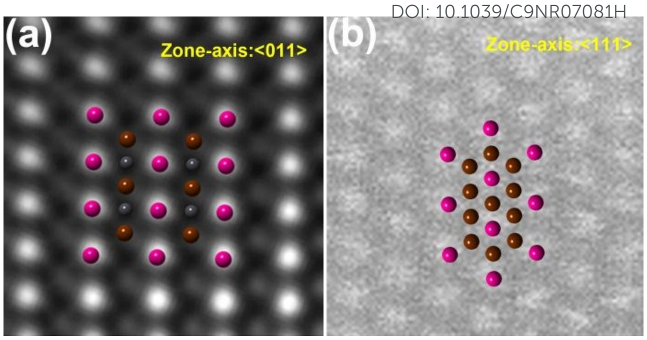

Figure 3. (a) Derived atomic structure (color balls) along the <0**1**1> zone-axis overlaid on a local HRTEM image (white and dark spots). (b) Derived atomic structure (color balls) along the <1**1**1> zone-axis. The background image was a local STEM image.

After doing a careful crystalline structure characterization and identification, we turn to discuss variable-temperature PL properties of the $CsPbBr_3$ PQDs embedded into a frozen methylbenzene solid. Figure 4 shows measured variable-temperature PL spectra of the $CsPbBr_3$ PQDs in the frozen methylbenzene solid under the excitation of a 325 nm He-Cd laser. Like in cases of other semiconductors, usual thermal quenching behavior was also observed in a temperature range of 5-180 K for the luminescence of $CsPbBr_3$ PQDs in the frozen solid. As seen in Figure 5(a), however, PL peak positions (solid circles) show abnormal almost independence on temperature in the interested temperature range. Note that the variable-temperature PL spectra shown in Figure 4 can be fitted very well with a standard Gaussian lineshape function.[26,27] By doing such lineshape fitting, we obtained PL FWHM data (solid triangles) at various temperatures, as shown in Figure 5(b). Also, FWHM data shows an anomalous nearly independence on temperature. When PL thermal quenching of the $CsPbBr_3$ PQDs may be understood in terms of thermal activation of non-radiative recombination centers,[28-30] the weak temperature dependence of both PL peak position and FWHM is a challenging abnormal behavior. Swarnkar *et al.* also observed that the PL peak positions of colloidal $CsPbBr_3$ nanocrystals do not alter with measurement temperature in the range of 25 to100 °C.[3] As argued below, we propose competing thermal activation mechanisms to interpret the abnormal almost temperature independence of the two major PL parameters.

View Article Online
DOI: 10.1039/C9NR07081H

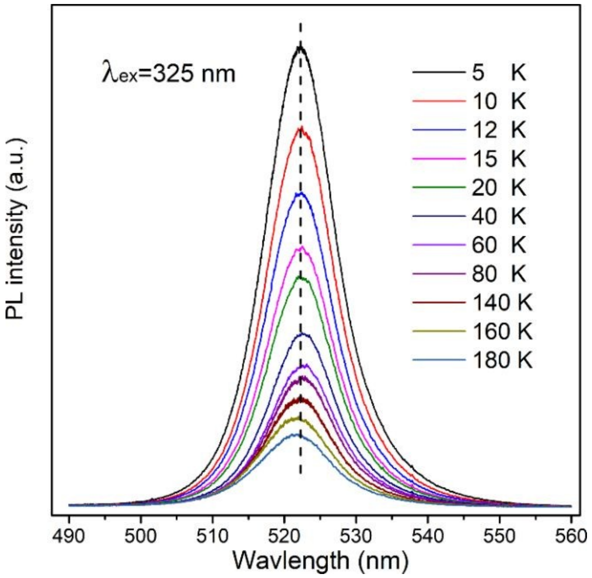

Figure 4. Variable-temperature PL spectra of $CsPbBr_3$ PQDs in frozen solid of methylbenzene at temperatures ≤ 180 K under the excitation of a 325 nm He-Cd laser. The vertical dashed line was drawn to guide eye.

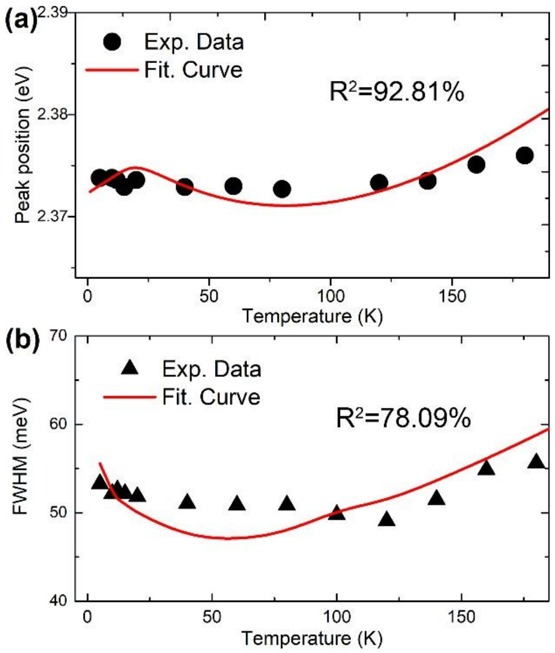

Figure 5. (a) Peak positions (solid circles) of the variable-temperature PL spectra of $CsPbBr_3$ QDs in frozen methylbenzene solid vs. temperature. The solid line represents a fitting curve with Eqs. (1) and (2) described in text. (b) FWHM (solid up triangles) of the variable-temperature PL spectra of $CsPbBr_3$ QDs in a frozen methylbenzene solid vs. temperature. The solid line represents a fitting curve with Eq. (3) described in text.

To elucidate the dependence of PL peak position on temperature, two major effects shall be taken into consideration. They are blue shift induced by thermal lattice expansion and red shift induced by thermal escaping of localized excitons from localization sites (e.g. $CsPbBr_3$ PQDs). For the former effect in $CsPbBr_3$ perovskite, it has been well argued by Yu and his co-workers,[30] concluding that the bandgap of perovskite semiconductors follows a positive linear dependence on temperature in a certain temperature range mainly due to thermal expansion of lattice. For the latter effect, the localized-states ensemble (LSE) luminescence model may be utilized to describe it.[31,32] By considering both effects, a quantitative description on temperature dependence of PL peak position may be formulated as

$$E(T) = E_g(0) + (A - x)\cdot k_B T\ , \qquad (1)$$

where $E_g(0)$ is the bandgap of perovskite semiconductor at 0 K, A is an adjustable parameter accounting for the thermal expansion induced blue shift, and x is a dimensionless coefficient which is usually a function of temperature and can be obtained by numerically solving the following nonlinear equation:[31,32]

$$xe^x = \left[\left(\frac{\sigma}{k_B T}\right)^2 - x\right]\left(\frac{\tau_r}{\tau_{tr}}\right)e^{(E_0 - E_a)/k_B T}. \qquad (2)$$

Definitions and physical meanings of the various parameters in Eq. (2) can be referred to the LSE luminescence model.[31,32] In Eq. (1) k_B is the Boltzmann constant, and T is absolute temperature.

By using Eqs. (1) and (2), we did a fitting to the temperature dependence of PL peak position, and the fitting result is illustrated by a solid line, as shown in Figure 5(a). Reasonably good agreement between experiment and fitting is achieved. Adopted parameters for the fitting are tabulated in Table 1. Note that E_0 in Eq. (2) is taken as $E_g(0) = 2.372$ eV in the fitting. As for temperature dependence of PL FWHM, spectral broadening effect induced by phonon scattering shall be taken into account. According to Rudin-Reinecke-Segall model,[33] phonon scattering shall include two terms, namely acoustic phonon scattering and LO phonon scattering in polar semiconductors. However, observed weak temperature dependence and even slight narrowing in PL FWHM in the temperature range of 5-150 K are challenging the consideration of only phonon broadening effect. We have to consider other competing mechanisms to compensate the phonon broadening mechanism. Thanks to the LSE model, the efficient thermal escaping of localized excitons,

View Article Online
DOI: 10.1039/C9NR07081H

especially those occupying at higher energetic states, can lead to an unique narrowing in PL linewidth as the temperature is increased.[32] Therefore, an overall temperature dependence of PL FWHM may be explicitly represented by

$$\Gamma = \Gamma_0 + \Gamma_c(T) + \sigma_A T + \gamma_{LO}[e^{\hbar\omega_{LO}/k_B T} - 1]^{-1}, \tag{3}$$

where $\mathit{\Gamma}_0$ is a constant accounting for the inhomogeneous broadening by imperfections, $\Gamma_c(T)$ is the narrowing term due to the thermal escaping of localized excitons, σ_A is an coefficient for the broadening by acoustic phonons, and γ_{LO} accounts for the broadening by LO phonons. $\hbar\omega_{\mathrm{LO}}$ represents the characteristic energy of LO phonons. A fitting curve with Eq. (3) is shown by solid line in Figure 5(b). Reasonably good agreement between experiment and fitting is achieved, as seen in Figure 6, when $\Gamma_0 = 9.02$ meV, $\sigma_A = 0.01\, meV/K$, $\gamma_{LO} = 11.61\, meV$, $\hbar\omega_{LO} = 20.01\, meV$, and the same other parameters as adopted in the fitting calculation of temperature dependence of peak positions are taken. Obtained LO phonon energy is well consistent with

Herein, let us give a brief discussion on $E_a - E_0$. In the LSE model, it is argued to give a measure of so-called average thermal activation energy or barrier.[32] Depending on materials and details of carrier localization, it can take positive or negative sign.[30,34] In the case of CsPbBr$_3$ PQDs in frozen methylbenzene solid, a thermal activation energy of 15.0 meV is obtained. This value is in good agreement with the activation energy (10-15 meV) of trapped excitons in CsPbCl$_3$ single perovskite crystal[35] and CsPbBr$_3$ nanocrystals.[36]

Table 1. Adopted parameters for the fitting calculation of Eq. (2).

Parameter	$E_a - E_0$	τ_r/τ_{tr}	σ	A
Value	15.0 meV	10	25.2meV	1.78

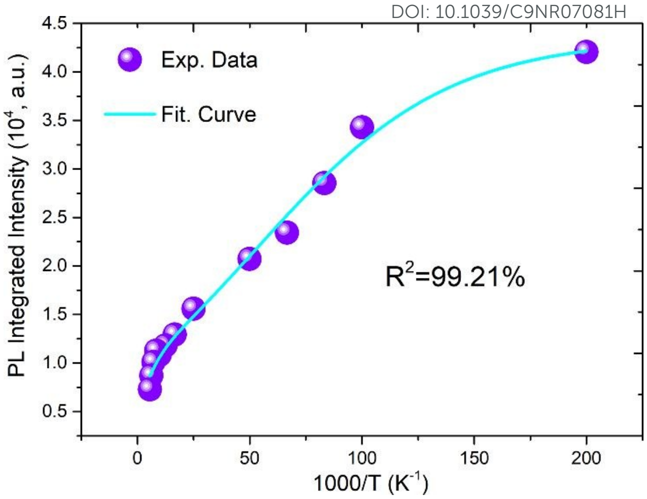

Figure 6. Arrhenius plot of the PL integrated intensity (solid balls) of CsPbBr$_3$ QDs in frozen methylbenzene solid. The solid line represents a fitting curve with Eq. (4) described in the text. R-squared value is also given in the figure.

Finally, we turn to discuss temperature dependence of the PL integrated intensity. Figure 6 depicts an Arrhenius plot of the integrated PL intensity (solid balls). The solid line is a fitting curve with a well-known two-step thermal quenching formula[24]

$$I = \frac{I_0}{1 + A_1 \mathrm{e}^{-\Delta E_1/\mathrm{k}_B T} + A_2 \mathrm{e}^{-\Delta E_2/k_B T}}, \tag{4}$$

in which I_0 is the PL integrated intensity at T=0 K, ΔE_1 and ΔE_2 denote two thermal activation energies. Solid line in Fig. 6 represents a fitting curve with Eq. (4), and the adopted parameters are shown in Table 2. The first thermal activation energy of ΔE_1=2.03 meV means that the PL quenches slow in the low temperature range, which may be attributed to the good confinement of excitons in the PQDs. The second larger thermal activation energy of ΔE_2=20.01 meV indicates faster quenching of the PL intensity in the higher temperature range. Note that the second larger thermal activation energy is well consistent with the value of $E_a - E_0 =$ 15 meV obtained previously. Both values are also in excellent agreement with the Raman value and the thermal activation energies obtained by us and other groups.[37,38] This might suggest that emission of LO phonons is a dominate process in the luminescence thermal quenching of the CsPbBr$_3$ PQDs embedded in frozen methylbenzene solid.[39]

Table 2. Adopted parameters for the fitting calculation using Eq. (4).

Paramete	I_0	ΔE_1	ΔE_2	A_1	A_2

DOI: 10.1039/C9NR07081H

r					
Value	4.348×10^4	2.03 meV	20.01 meV	3.46	3.5443

3. CONCLUSIONS

Crystalline structure characterization and variable-temperature PL spectra of $CsPbBr_3$ PQDs synthesized with a facile room-temperature solution-processed approach are presented in this study. For the crystalline structure of PQDs, it is unveiled to take a cubic phase by using multiple techniques of HRTEM + SAED + STEM + simulation. Anomalous weak temperature dependence is observed for both PL peak position and linewidth of the $CsPbBr_3$ PQDs incorporated into a frozen methylbenzene solid in the interested temperature range of 5-180 K. We propose some competing mechanisms to quantitatively interpret the anomalous thermal behaviors of both key PL spectral parameters for the first time. Good agreement between experiment and model fitting provides an unprecedented understanding of luminescence mechanism of $CsPbBr_3$ PQDs randomly embedded into organic solid matrix.

4. EXPERIMENTAL SECTION

4.1 Synthesis of $CsPbBr_3$ QDs

Figure 7 schematically shows key procedures for the solution-based preparation of $CsPbBr_3$ perovskite QDs at room temperature. To synthesize the PQDs, commercially available CsBr (99.9 %, J&K Scientific) and $PbBr_2$ (99.999 %, J&K Scientific) powders were accurately weighted in accordance with stoichiometric ratio of 1:1. We dissolved the mixture of CsBr and $PbBr_2$ powders into dimethyl formamide (DMF, 99.9%, Aladdin) followed by vigorous stirring operation to form a uniform solution. Then, a certain amount of OA (AR, Aladdin) and OAm (80-90%, Aladdin) liquids was dropped into the above solution under the continuous stirring for 30 min. Herein, OA and OAm serve as surface ligands. Next, a little amount of above obtained solution was added into 2 mL toluene under the stirring operation. Due to the extremely low solubility of source materials in this solvent, oversaturated solution forms subsequently followed by the crystallization and generation of PQDs. The chemical reaction may be written as: $CsBr+PbBr_2\rightarrow CsPbBr_3$. Nanocrystal size of $CsPbBr_3$ PQDs was mainly determined by the dropping concentration of source materials. In order to yield PQDs powder, the above-described PQDs solution was firstly centrifuged at a high speed of 1200 rpm with the precipitation of PQDs at the bottom. Then, the upper solvent was removed and the obtained precipitation of PQDs was washed for three times with anhydrous ethanol. Followed by vacuum drying process at 80 °C for 10 hrs, yellowish PQDs powder was obtained. Note that all these solution-based preparation procedures were carried out at room temperature of 25 °C. This facile approach is thus suitable for massive fabrication of $CsPbBr_3$ PQDs.

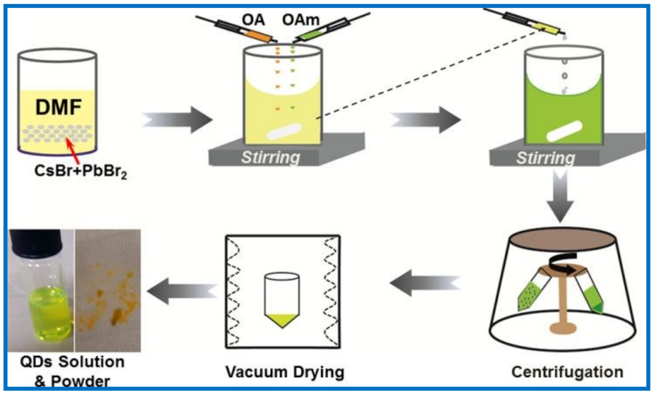

Figure 7. Schematic illustration of synthesizing all-inorganic $CsPbBr_3$ PQDs at room temperature with a full solution approach.

4.2 Characterization methods

Crystalline structural characterization was conducted on JEOL Model JEM-2011 TEM equipment with functions of high-resolution TEM plus SAED, as well as STEM. Single crystal software was used to simulate the obtained experimental results. Variable-temperature PL spectra were measured on a home-assembled PL setup composed of a high-resolution 1200 l/mm grating monochromator (Spex 750M) and a photomultiplier tube (Hamamatsu R928).[40] Sample temperature was precisely controlled from 5 K to 300 K via a Lakeshore temperature controller with a closed cycle refrigerator (Janis Shi cryostat). A lock-in amplifier (Stanford Research SR830) together with a standard optical chopper was employed to enhance the signal-to-noise ratio. PL data were recorded by a PC via data acquire module converting analog signal into digital data.

Notes

The authors declare no competing financial interest.

Acknowledgments

View Article Online
DOI: 10.1039/C9NR07081H

This work was supported by National Natural Science Foundation of China (Grant No. 11374247) and HKU SRT on New Materials. One of the authors, F.T. wishes to thank Mr. J. Mao and Prof. Wallace Choy for their help and kindness in the preparation of $CsPbBr_3$ perovskite QDs.

References

1 Z. Ning, X. Gong, R. Comin, G. Walters, F. Fan, O. Voznyy, E. Yassitepe, A. Buin, S. Hoogland, E. H. Sargent, *Nat.* **2015**, 523, 324–328.
2 X. Gong, Z. Yang, G. Walters, R. Comin, Z. Ning, E. Beauregard, V. Adinolfi, O. Voznyy, E. H. Sargent, *Nat. Photo.* **2016**, 10, 253–257.
3 A. Swarnkar, R. Chulliyil, V. K. Ravi, M. Irfanullah, A. Chowdhury, A. Nag, *Angew. Chem.* **2015**, 127, 15644–15648.
4 J. Song, J. Li, X. Li, L. Xu, Y. Dong, H. Zeng, *Adv. Mater.* **2015**, **27**, 7162–7167.
5 N. J. Jeon, J. H. Noh, W. S. Yang, Y. C. Kim, S. Ryu, J. Seo, S. I. Seok, *Nat.* **2015**, 517, 476–480.
6 Y. Fu, H. Zhu, C. Stoumpos, Q. Ding, J. Wang, M. G. Kanatzidis, X. Zhu, S. Jin, *ACS Nano* **2016**, 10, 7963–7972.
7 L. Protesescu, S. Yakunin, M. I. Bodnarchuk, F. Krieg, R. Caputo, C. H. Hendon, R. X. Yang, A. Walsh, M. W. Kovalenko, *Nano Lett.* **2015**, 15, 3692–3696.
8 X. Zhang, B. Xu, J. Zhang, Y. Gao, Y. Zheng, K. Wang, X. W. Sun, *Adv. Funct. Mater.* **2016**, 26, 4595–4600.
9 G. E. Eperon, G. M. Paternò, R. J. Sutton, A. Zampetti, A. A. Haghighirad, F. Cacialli, H. J. Snaith, *J. Mater. Chem. A* **2015**, 3, 19688–19695.
10 M. Becker, R. Vaxenburg, G. Nedelcu, P. C. Sercel, A. Shabaev, M. J. Mehl, J. G. Michopoulos, S. G. Lambrakos, N. Bernstein, J. L. Lyons, T. Stöferle, R. F. Mahrt, M. V. Kovalenko, D. J. Norris, G. Rainò, A. L. Efros, *Nat*. **2018**, 553, 189-193.
11 Y. H. Song, J. S. Yoo, B. K. Kang, S. H. Choi, E. K. Ji, H. S. Jung, D. H. Yoon, *Nanoscale* **2016**, 8, 19523–19526.
12 H.–C. Wang, S.–Y. Lin, A.–C. Tang, B. P. Singh, H.–C. Tong, C.–Y. Chen, Y.–C. Lee, T.–L. Tsai, R.–S. Liu, A*ngew. Chem. Int. Ed.* **2016**, 55, 7924–7929.
13 J. Shamsi, P. Rastogi, V. Caligiuri, A. L. Abdelhady, D. Spirito, L. Manna, R. Krahne, *ACS Nano* **2017**, 11, 10206–10213.
14 Q. Zhang, Y. Yin, *ACS Cent. Sci.* **2018**, 4, 668–679.
15 J. Kang, L.–W. Wang, *J. Phys. Chem. Lett.* **2017**, 8, 489–493.
16 J. Huang, M. Lai, J. Lin, P. Yang, *Adv. Mater.* **2018**, 30, e1802856.
17 P. Cottingham, R. L. Brutchey, *Chem. Commun.* **2016**, 52, 5246–5249.
18 M. C. Brennan, M. Kuno, S. Rouvimov, *Inorg. Chem.* **2019**, 58, 1555–1560.
19 Y. Yu, D. Zhang, C. Kisielowski, L. Dou, N. Kornienko, Y. Bekenstein, A. B. Wong, A. P. Alivisatos, P. Yang, *Nano Lett.* **2016**, 12, 7530–7535.
20 J. He, A. Towers, Y. Wang, P. Yuan, Z. Jiang, J. Chen, A. J. Gesquiere, S.–T. Wu, Y. Dong, *Nanoscale* **2018**, 10, 15436–15441.
21 F. Zhang, Z.-F. Shi, Z.-Z. Ma, Y. Li, S. Li, D. Wu, T.-T. Xu, X.-J. Li, C.-X. Shan, G.-T. Du, *Nanoscale* **2018**, 10, 20131–20139.
22 S. Utsunomiya, M. Kogawa, E. Kamiiski, R. C. Ewing, Actinide Nanoparticle Research, ed. by S. N. Kalmykov and M. A. Denecke, (Springer–Verlag Berlin Heidelberg 2011), Chap. 2, pp. 33–62.
23 D. S. He, Z. Y. Li, J. Yuan, *Micron* **2015**, 74, 47–53.
24 J. L. Lábár, *Ultramicroscopy* **2005**, 103, 237-249.
25 D. Palmer, Crystal Maker Software Ltd, Oxfordshire, England, 2012.
26 Z. F. Shi, Y. Li, Y. T. Zhang, Y. S. Chen, X. J. Li, D. Wu, T. T. Xu, C. X. Shan, and G. T. Du, *Nano Lett.* **2017**, 17, 313–321.
27 M. Leroux, N. Grandjean, B. Beaumont, G. Nataf, F. Semond, J. Massies, P. Gibart, *J. Appl. Phys.* **1999**, 86, 3721–3728.
28 Z. F. Wei, S. J. Xu, R. F. Duan, Q. Li, J. Wang, Y. P. Zeng, H. C. Liu, *J. Appl. Phys*. **2005**, 98, 084305.
29 Y. Zhao, C. Riemersma, F. Pietra, R. Koole, C. de Mello Donegá, A. Meijerink, *ACS Nano* **2012**, 6, 9058–9067.
30 C. Yu, Z. Chen, J. J. Wang, W. Pfenninger, N. Vockic, J. T. Kenney, K. Shum, *J. Appl. Phys.* **2011**, 110, 063526.
31 Q. Li, S. J. Xu, W. C. Cheng, M. H. Xie, S. Y. Tong, C. M. Che, H. Yang, *Appl. Phys. Lett.* **2001**, 79, 1810−1812.
32 Q. Li, S. J. Xu, M. H. Xie, S. Y. Tong, *Europhys. Lett.* **2005**, 71, 994–1000.
33 S. Rudin, T. L. Reinecke, B. Segall, *Phys. Rev. B* **1990**, 42, 11218–11231.
34 Q. Li, S. J. Xu, M. H. Xie, S. Y. Tong, *J. Phys: Conden. Matter* **2005**, 17, 4853–4858.
35 M. Nikl, E. Mihokova, K. Nitsch, K. Polak, M. Rodova, M. Dusek, G. P. Pazzi, P. Fabeni, L. Salvini, M. Gurioli, *Chem. Phys. Lett*. **1994**, 220, 14−18.

View Article Online
DOI: 10.1039/C9NR07081H

36 A. Dey, P. Rathod, D. Kabra, *Adv. Opt. Mater*. **2018**, 6, 1800109.

37 C. Wolf, T.–W. Lee, *Mater. Today Energy* **2018**, 7, 199-207.

38 X. Lao, Z. Yang, Z. Su, Y. Bao, J. Zhang, X. Wang, X. Cui, M. Wang, X. Yao, S. Xu, *J. Phys. Chem. C* **2019**, 123, 5128–5135.

39 C. W. Struck,·W. H. Fonger, *Inorganic Chemistry Concepts*, v. 13 (Springer–Verlag Berlin Heidelberg 1991)

40 S. J. Xu, W. Liu, M. F. Li, *Appl. Phys. Lett*. **2000**, 77, 3376–3378.

View Article Online
DOI: 10.1039/C9NR07081H